doi:10.26443/seismica.v1i1.197

The Root to the Galápagos Mantle Plume on the Core-Mantle Boundary

Sanne Cottaar *[1], **Carl Martin** [1], **Zhi Li** [1], **Rita Parai** [2]

[1]Department of Earth Sciences, University of Cambridge, Cambridge, UK , [2]Department of Earth and Planetary Sciences, Washington University in St Louis, St Louis, MO, USA

Author contributions: *Conceptualization*: SC. *Methodology*: SC, CM, ZL. *Investigation*: SC, CM, RP. *Visualization*: SC, CM. *Writing – original draft*: SC, RP. *Writing – review & editing*: SC, CM, ZL, RP.

Abstract Ultra-low velocity zones (ULVZs) are thin anomalous patches on the boundary between the Earth's core and mantle, revealed by their effects on the seismic waves that propagate through them. Here we map a broad ULVZ near the Galápagos hotspot using shear-diffracted waves. Forward modeling assuming a cylindrical shape shows the patch is ~600 km wide, ~20 km high, and its shear velocities are ~25% reduced. The ULVZ is comparable to other broad ULVZs mapped on the core-mantle boundary near Hawaii, Iceland, and Samoa. Strikingly, all four hotspots where the mantle plume appears rooted by these 'mega-ULVZs', show similar anomalous isotopic signatures in He, Ne, and W in their ocean island basalts. This correlation suggests mega-ULVZs might be primordial or caused by interaction with the core, and some material from ULVZs is entrained within the plume. For the Galápagos, the connection implies the plume is offset to the west towards the base of the mantle.

Production Editor: Gareth Funning
Handling Editor: Lauren Waszek
Copy & Layout Editor: Théa Ragon

Received: July 1, 2022
Accepted: September 20, 2022
Published: October 28, 2022

Non-technical summary Observations of deep-diving earthquake waves reveal heterogeneity and dynamics within the Earth. Here we use waves that diffract along the boundary between the core and the mantle to map a patch of anomalous material on top of the boundary. The waves propagating within the patch are slowed down by 25% compared to those propagating in surrounding material, and the waves are refracted when entering and exiting the patch. These waves arrive at seismic stations delayed by tens of seconds. By modeling the waveforms, and mapping the directionality of this delayed energy, we constrain the location of the patch beneath the eastern Pacific and to the west of the Galápagos archipelago. The patch can be approximated as a cylinder with a width of 600 km and height of 20 km. Such patches are named ultra-low velocity zones or ULVZs. Similar large ULVZs are found near other intraplate volcanic hotspots, i.e. Hawaii, Iceland and Samoa. Volcanic basalts on these islands and the Galápagos show anomalous isotopic signatures, which could be dragged up in a mantle plume from the ULVZ at the core-mantle boundary and indicate that the material within the ULVZs was either created early in Earth's history or contains material leaking from the core.

1 Introduction

The lowermost hundreds of kilometers of the mantle are the lower thermal boundary layer in mantle dynamics, which is partially driven by heat flow across the core-mantle boundary. The layer plays a major role in Earth's thermal and dynamical history. Seismic waves have revealed it is characterized by strong lateral variations in seismic wave speed, which are linked to variations in temperature and composition. On the global scale, there are two widespread regions with relatively slow seismic velocities, dubbed Large Low Velocity Provinces (LLVPs, e.g. Cottaar and Lekić, 2016; Garnero et al., 2016), which are surrounded by regions of relatively fast seismic velocities that can be interpreted as the accumulation of subducted tectonic plates or slabs (e.g. Domeier et al., 2016; Hilst et al., 1997). Much thinner in nature, on the order of 10s of km, but more extreme in their velocity anomaly, are the ultra-low velocity zones (ULVZs). ULVZs appear patchy in nature and are directly on the core-mantle boundary. While only a fraction of the core-mantle boundary has been targeted for these anomalies, there is a weak trend that these patches appear within or near the LLVPs (Yu and Garnero, 2018). In studies that produce ULVZ probability maps using a single data type over a large swath of the core-mantle boundary, this trend is disputed (Thorne et al., 2020, 2021). However, the appearance of ULVZs within LLVPs is certainly true for the broadest of ULVZs that have been mapped in 3D (Cottaar and Romanowicz, 2012; Thorne et al., 2013; Yuan and Romanowicz, 2017; Jenkins et al., 2021; Krier et al., 2021; Lai et al., 2022; Li et al., 2022), and can be dubbed 'mega-ULVZs' after Thorne et al. (2013). The three mega-ULVZs currently mapped lie in the vicinity of the Hawaiian, Icelandic and Samoan hotspots, and such large structures appear otherwise rare, at least across a large swath of the Pacific (Kim et al., 2020). Suggestions of the presence of other mega-ULVZs have been made be-

*Corresponding author: sc845@cam.ac.uk

low Marquesas and Caroline hotspots (Kim et al., 2020; Thorne et al., 2021), but these have not been mapped to the same detail.

The nature and origin of ULVZs are uncertain. Their velocity reductions are so extreme that their composition must be anomalous, and enrichment of magnesiowüstites is a prime candidate (Wicks et al., 2017; Dobrosavljevic et al., 2019). The presence of partial melt is also proposed, but is unlikely to form stable ULVZs as the melt is dense due to enriched in Fe and drains to the core-mantle boundary (Hernlund and Jellinek, 2010; Dannberg et al., 2021). Solid-state ULVZs could be remnants of an early molten mantle, becoming enriched in magnesiowüstite due to fractional crystallization, and therefore have a primordial origin (Labrosse et al., 2007). The potential of Fe-enrichment by the core has also been proposed, through mechanisms of diffusion (Hayden and Watson, 2007; Lesher et al., 2020) or mechanisms driven by morphological instabilities (Kanda and Stevenson, 2006; Otsuka and Karato, 2012; Lim et al., 2021). If ULVZs are dense in composition, questions remain as to whether they are passive markers of surrounding convection (Li et al., 2017, 2022), play an active role by rooting mantle plumes (Jellinek and Manga, 2004), and if their material can be entrained in plumes (Jones et al., 2019).

Here we present evidence for the presence of a mega-ULVZ on the core-mantle boundary to the west of the Galápagos hotspot using shear diffracted waves. Shear diffracted energy incident upon a mega-ULVZ, causes guided waves within. This energy is refracted due to the velocity contrast at the entry to and exit from the ULVZ. At a seismic station, the refracted energy arrives off-angle and delayed by 10s of seconds. We refer to this as the 'Sdiff postcursor'. The frequency content of the postcursors is sensitive to the height of the ULVZ. Their delay times are sensitive to the size, shape, and velocity reduction of the ULVZ. We focus on four earthquakes with Sdiff postcursors sampling the core-mantle boundary near the Galápagos Islands. Our preferred ULVZ model is found by synthetic waveform modeling for 3D ULVZ models, and by imaging the directionality of the postcursor energy.

2 Data and Methods

2.1 Data Catalogue

Recognizing consistent arrivals of Sdiff postcursors caused by a mega-ULVZ requires dense data coverage. The Transportable Array (TA) is a large-scale deployment of 400 seismic stations that has gradually moved from west to east across the conterminous United States between 2004 and 2015 with a rough station spacing of 70 km. The presence of the TA here played a major role in the discovery and mapping of the Hawaiian, Samoan and Icelandic mega-ULVZs (Cottaar and Romanowicz, 2012; Thorne et al., 2013; Yuan and Romanowicz, 2017). Over several years since 2014, the TA was transferred to Alaska, monitoring the most seismically active state of the US with unprecedented coverage, while also providing new geometries to study the core-mantle boundary. Observations of Sdiff waves from Chilean earthquakes to the Alaska TA provided us with the first evidence of the presence of Sdiff postcursors caused by a ULVZ beneath the eastern Pacific. Subsequently, we built a catalogue of postcursor observations.

We visually assess earthquake data for the presence of Sdiff postcursors caused by a ULVZ near the Galápagos Islands from a globally compiled data set of Sdiff phases for all earthquakes over a magnitude of 5.7 and for all depth ranges. Data are filtered between 10 and 30 s. To assess, Sdiff phases are aligned on their predicted arrival time and organized as a function of azimuth. A postcursor is recognized by strong later arrival that has a move-out in time as a function of azimuth with respect to the main Sdiff arrival. They can only be observed if there is sufficient data coverage, a good signal-to-noise ratio (judged by eye), and no strong interfering depth phases. A catalogue of promising observations of postcursors caused by the Galápagos ULVZ is given in Table S1. We focus on four high quality events that sample the Galápagos ULVZ from a variety of angles. For these events, we quality check the data by eye, and remove traces with low signal-to-noise ratio. Several further examples of postcursor observations are presented in the supplementary materials.

2.2 Forward modeling

We compute full waveform synthetics for 3D ULVZ models using the 'sandwiched' version of the Coupled Spectral Element Method (sandwiched-CSEM, Capdeville et al., 2002, 2003), similar to Cottaar and Romanowicz (2012) and Yuan and Romanowicz (2017). The 'sandwiched'-CSEM computes the spectral element solution for a full 3D model in the lowermost 370 km of the mantle, and couples this to a normal mode summation for a 1D model in the rest of the mantle and the core. This method allows for relative computational efficiency to compute synthetics down to periods of 10 seconds for a finely meshed model in the lowermost mantle, at the cost of not having a fully 3D model in the rest of the planet. The internal SEM mesh is defined to have a boundary at the top of the ULVZ.

To reduce the parameter space to search, we assume a cylindrical anomaly for which we determine the radius, height, shear wave velocity reduction, and location in latitude and longitude. Computing full-waveform synthetics is too computationally expensive to allow for a full grid search of all five parameters. Instead, we evaluate the delays, move-outs and amplitudes of resulting postcursors by eye, and adjust the model to approach a better fit.

In the background, we use the radially anisotropic shear velocities of SEMUCB-WM1 (French and Romanowicz, 2014), and a scaled P-wave model. Both models are tapered to the background 1D model in the top 70 km of the SEM mesh. Inside the ULVZ, the isotropic shear wave velocities are reduced. The Vp reduction is scaled by a factor of 1, but this choice has negligible effect on the Sdiff waveforms. The density deviation is scaled by a factor of -0.5, and is thus increased within the ULVZ, but again has little effect on the Sdiff

	Date	Depth [km]	Lat. [°N]	Long.[°W]	M_w	Location
A	2016/12/25	21.5	-43.41	-73.94	7.6	Southern Chile
B	2019/09/29	16.7	-35.56	-73.10	6.7	Off Coast of Central Chile
C	2015/05/19	14.9	-54.53	-132.39	6.6	Pacific-Antarctic Ridge
D	2017/02/24	417.9	-23.44	-178.77	7.0	South of Fiji Islands

Table 1 Parameters for the earthquakes. All earthquake parameters are from the Global Centroid-Moment Tensor project (Ekström et al., 2012) except for event A, for which the W-phase solution published by the USGS National Earthquake Information Centre provided a better waveform fit. See Table S1 for full catalogue.

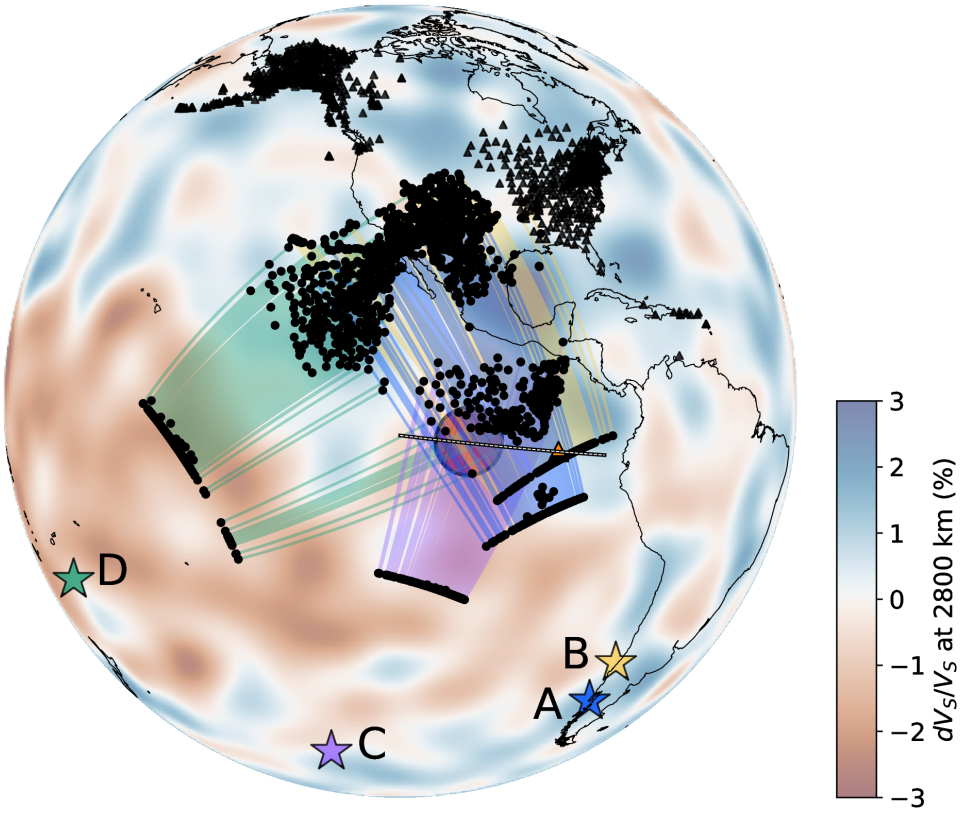

Figure 1 Map shows the geometry of the shear diffracted waves. Data geometries are shown by earthquake location (star), station locations (grey triangles), and ray path sensitivity to the core-mantle boundary (shaded regions between piercing points at 2800 km depth). Earthquake locations and ray paths are colored per event: A-blue, B-yellow, C-purple, and D-green. For earthquake parameters, see Table 1. The Galápagos hotspot is indicated by an orange triangle. The location of the Galápagos ULVZ, as constrained in this study, is shown as the red-filled circle. Background model is showing the shear wave velocity deviations at 2800 km depth from the tomographic SEMUCB-WM1 (French and Romanowicz, 2014). Black line with white dash shows the geometry of the cross-sections in Fig. 8.

waveforms.

2.3 Beamforming

Using arrays of seismic stations, we can determine the directionality of incoming energy. Searching over the incoming backazimuth is called beamforming, while searching over the slowness or incident angle is called slant-stacking (or vespa processing, e.g. Rost and Thomas, 2002). Shear diffracted waves have a predicted slowness of 8.32 s/dg for PREM (Dziewonski and Anderson, 1981), but this could vary due to the velocities in the lowermost mantle at the location where the energy propagates upwards to the seismic array. The slowness, or incident angle, could vary slightly between the main wave and the postcursor when they come from different directions. For these reasons, we do not fix the slowness when beamforming, but search over coherent energy by stacking the signals, $s_j(t)$, as a function of time t, slowness, u_{hor}, and backazimuth, θ, for a given subarray,

$$S\left(t, u_{hor}, \theta\right) = \sum_{j=1}^{N} s_j\left(t - u_{hor}(\theta) \cdot x_j\right) \tag{1}$$

where $u_{hor}(\theta) = u_{hor}\begin{pmatrix}\sin\theta\\ \cos\theta\end{pmatrix} = \begin{pmatrix}u_{EW}\\ u_{NS}\end{pmatrix}$ is the horizontal slowness vector, and $x_j = \begin{pmatrix}x_{EW}\\ x_{NS}\end{pmatrix}_j$ is the distance vector to the centre of the subarray.

A seismic signal can be expressed in amplitude and instantaneous phase:

$$s_j(t) = A_j(t)\exp\left[i\Phi_j(t)\right] \tag{2}$$

We create two separate stacks, one stack for the amplitude envelope, S_A, setting $s_j(t) = A_j(t)$, and one

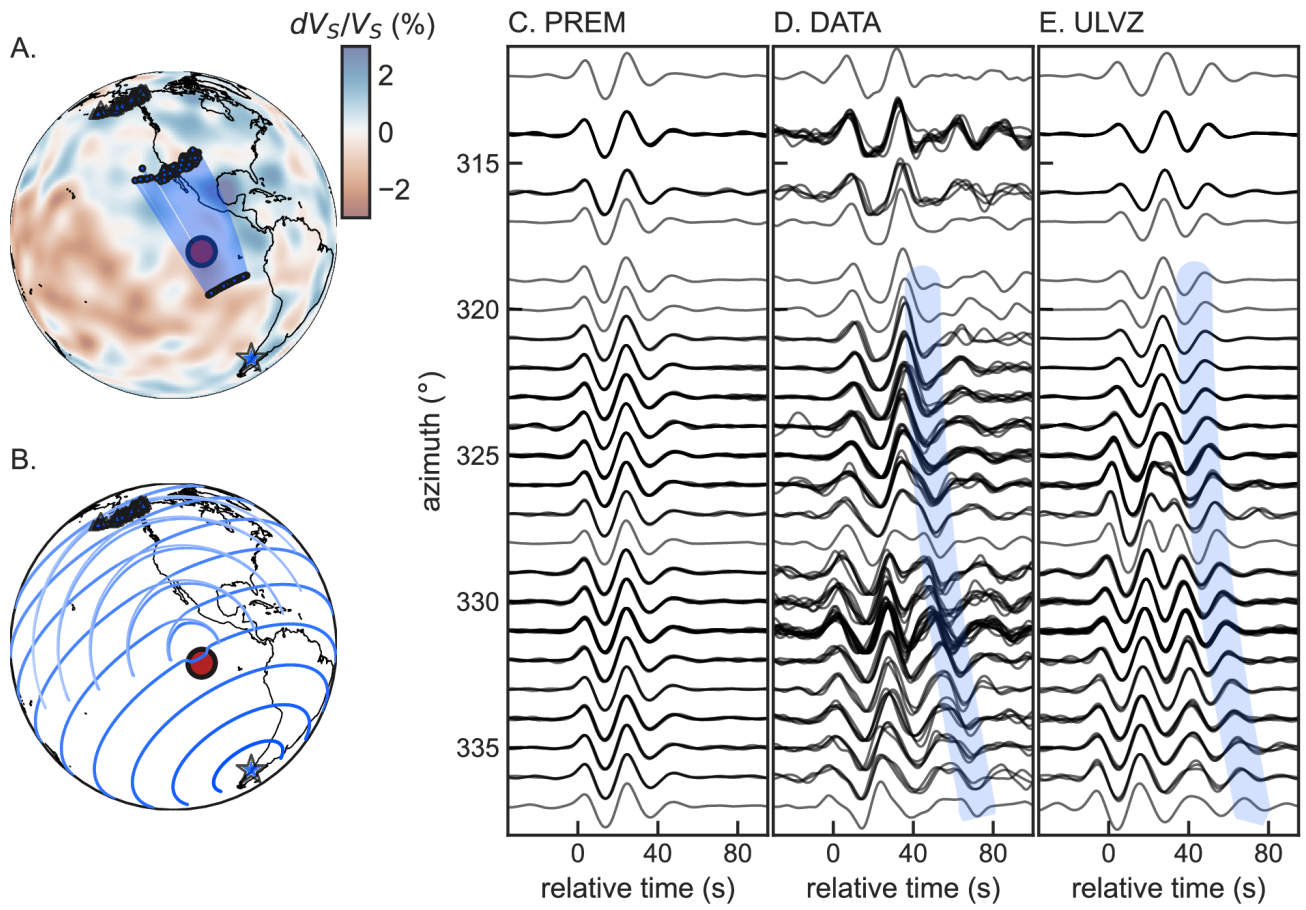

Figure 2 Geometry, data, and synthetics for event A. (A) Geometry of data coverage, event (star), stations (triangles), and sensitivity to the core-mantle boundary (shaded region) and ULVZ model (red circle). Background shows the shear wave velocity deviations at 2800 km depth from the tomographic SEMUCB-WM1 (French and Romanowicz, 2014). (B) Wavefront predictions for modeled ULVZ illustrating the cause of the postcursors. For an animation, see Movie S1. (C) Synthetic waveforms for 1D Earth model PREM (Dziewonski and Anderson, 1981). (D) Observed data. (E) Synthetics including background tomographic model and the preferred cylindrical ULVZ model. Data panels show SHdiff on the transverse component filtered between 10 and 30 s, binned by azimuth and centered on the predicted arrival times. Postcursor energy is highlighted by shaded region.

stack over the phase, S_Φ, setting $s_j(t) = \exp[i\Phi_j(t)]$. Finally, we interpret a phase weighted envelope stack (Schimmel and Paulssen, 1997), where the phase is weighted by a factor of 4,

$$PWES = S_A {S_\Phi}^4 \tag{3}$$

where all stacks are 3D arrays as a function of (t, u_{hor}, θ).

A light Gaussian filter is applied to the stack to reduce irregularities and allow automated picking of peaks. The main peak and other peaks above 10% of the maximum peak are picked. Uncertainty is established by taking the minimum and maximum values for the contour at 95% of the peak amplitude. An example of a high-quality stack is shown in Fig. S13.

To build subarrays for an event, we create a sliding window in distance-azimuth space. The window is both 5° in distance and in azimuth, and we shift the window every 2° in azimuth and distance. For each window that has at least 12 stations, a stack is considered. The stacks are manually quality controlled for having one or two clear peaks that are well constrained in time-slowness-backazimuth space.

3 Results

3.1 Sdiff postcursor data set

Our analyses are based on waveform data from four different earthquakes (Fig. 1, Table 1). We use shear-diffracted waves recorded at the Alaska TA from two major earthquakes in Chile that sample the core-mantle boundary beneath the Eastern Pacific (Events A and B). Events A and B are shallow thrust events along the Chilean subduction zone of magnitude 7.6 on 25 December 2016 and magnitude 6.7 on 29 September 2019, respectively.

With Sdiff observations from only one azimuthal direction, the location of the ULVZ in the direction of their propagation remains non-unique. To fully constrain the location of ULVZs, we need rays crossing at a different angle. This is provided by Event C, which is a magnitude 7.2 on the Pacific-Antarctic ridge, recorded in the north-eastern US and south-eastern Canada. Additional evidence from a third angle comes from recordings across the Caribbean for an event in Fiji, although coverage in this direction is poor (Event D).

Figs. 2-5 show the expected and observed data for

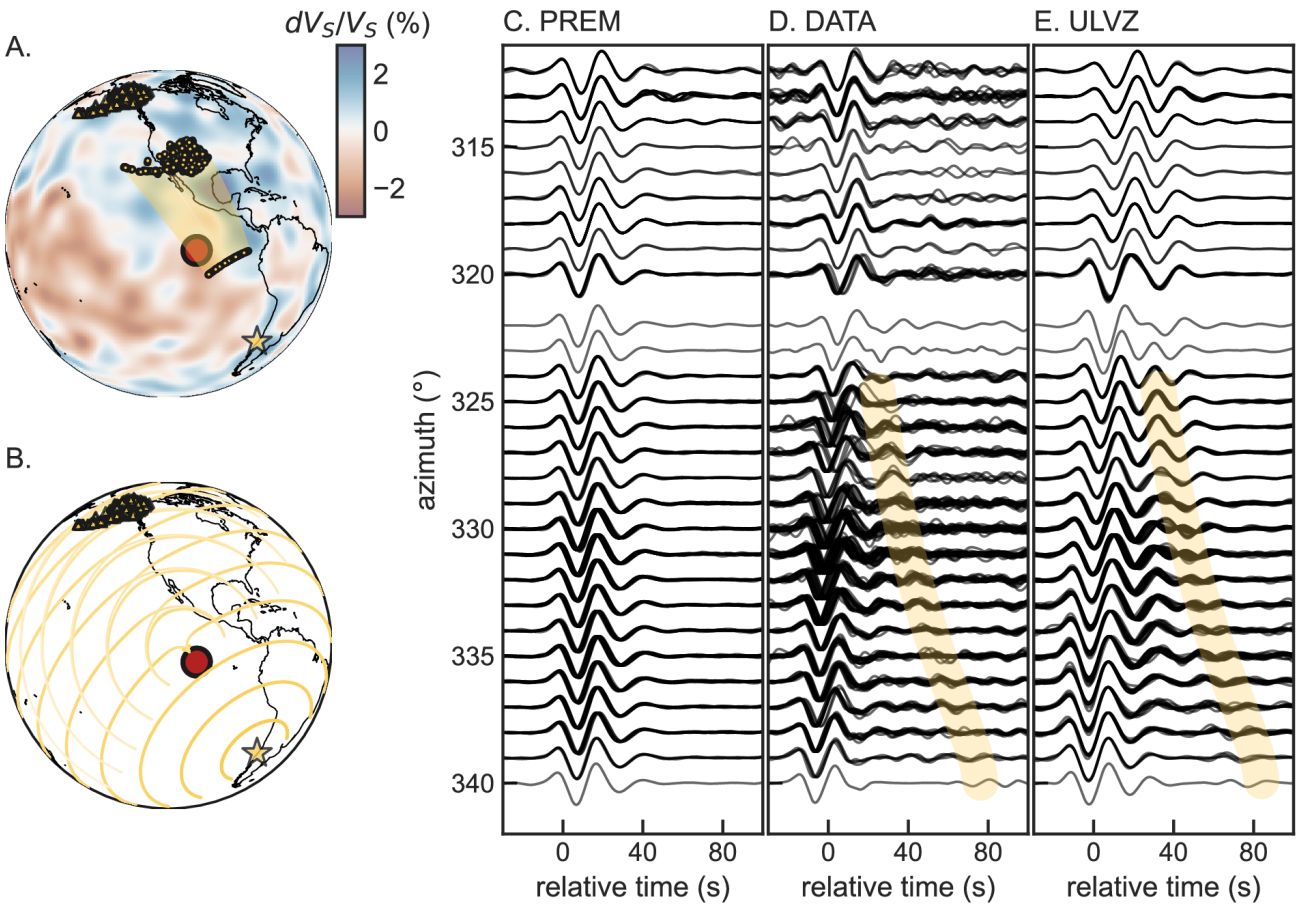

Figure 3 Geometry, data, and synthetics for event B. Same as Figure 2, but for Event B. For an animation, see Movie S2.

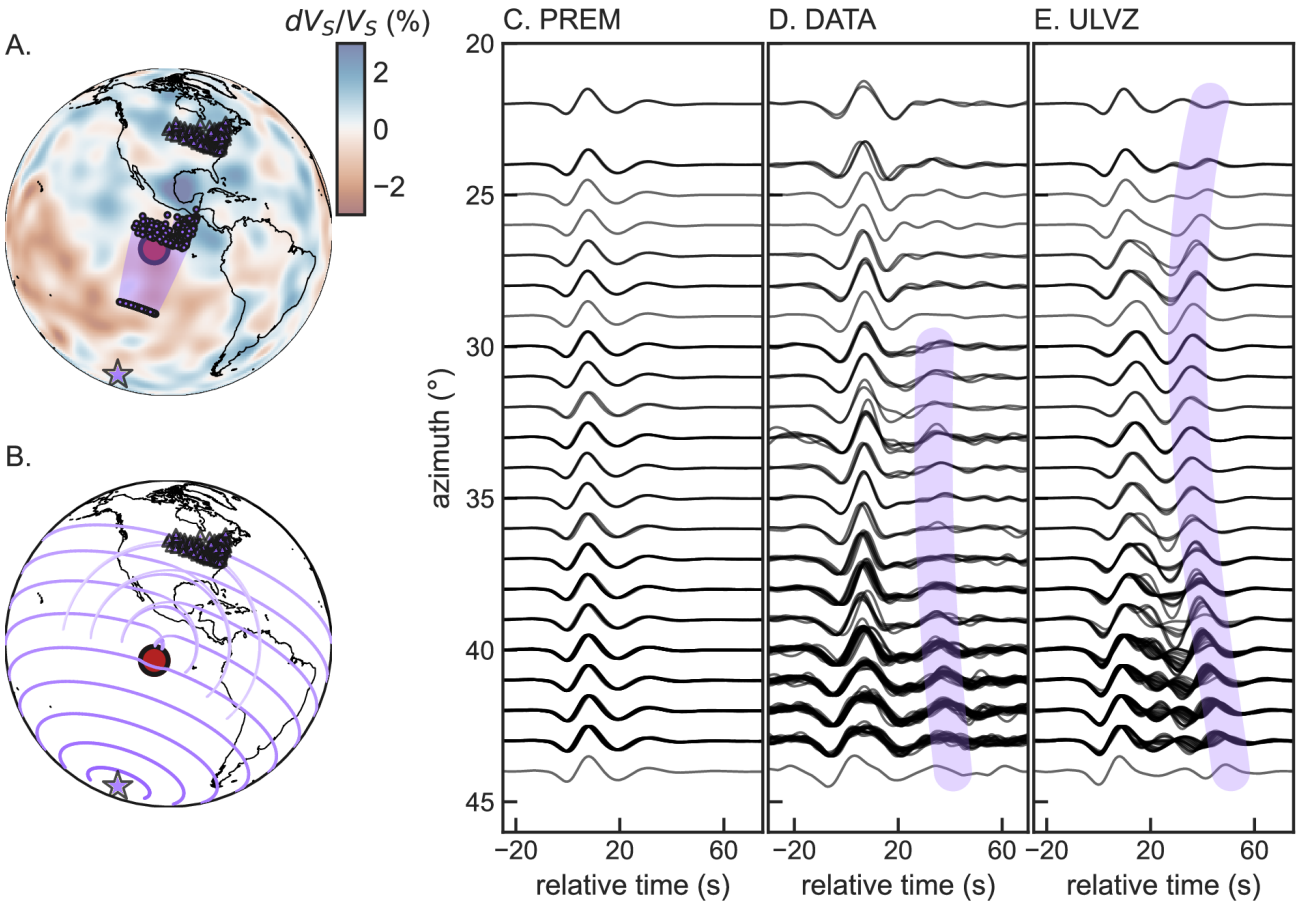

Figure 4 Geometry, data, and synthetics for event C. Same as Figure 2, but for Event C. For an animation, see Movie S3.

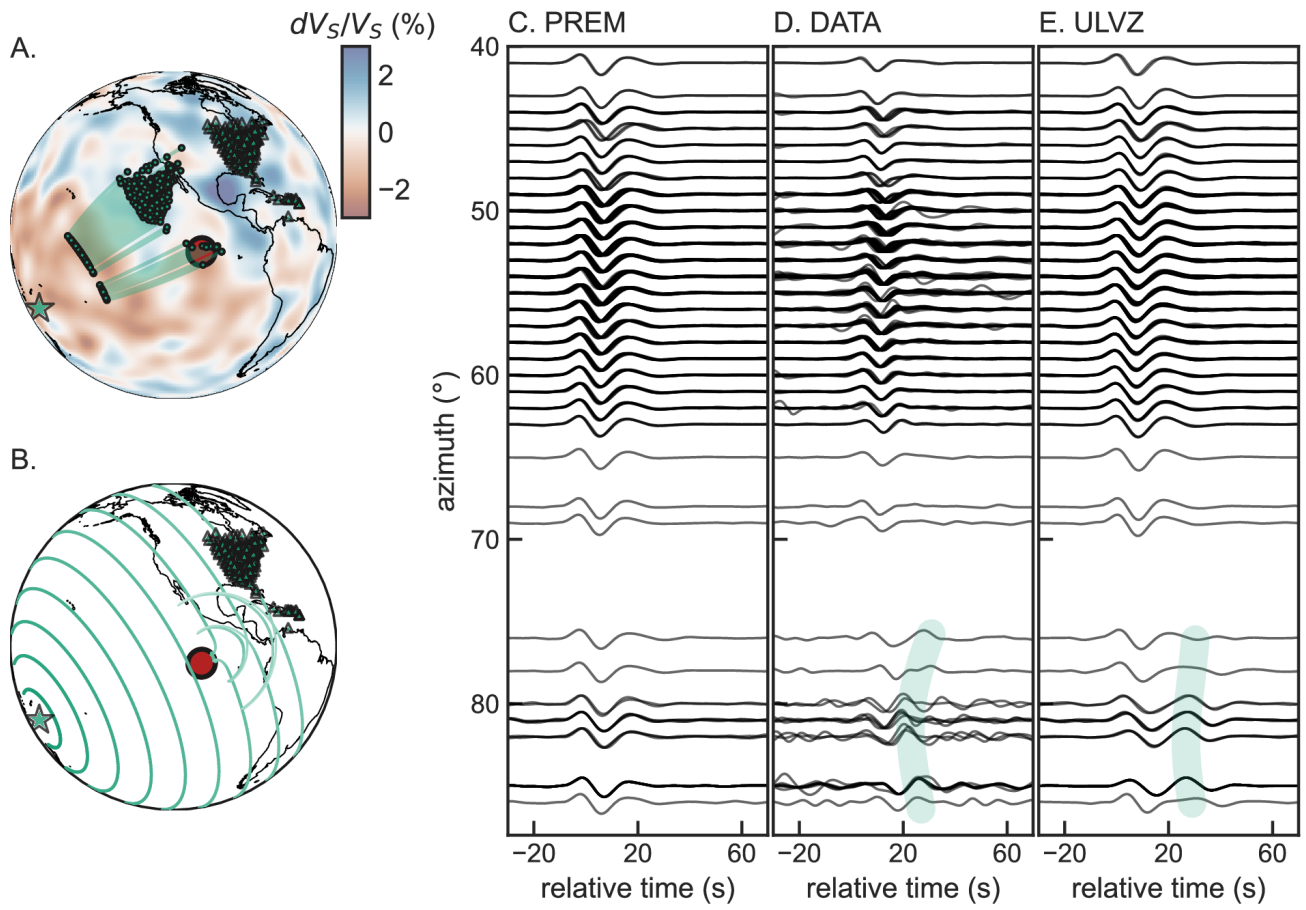

Figure 5 Geometry, data, and synthetics for event D. Same as Figure 2, but for Event D. For an animation, see Movie S4.

events A-D. The SH component of the shear diffracted wave and its postcursor attenuates less along the core-mantle boundary and therefore these phases are best observed on the transverse component. Transverse components shown are bandpass filtered between periods of 10 and 30s. Data are organized as a function of azimuthal angle from the earthquake and windowed around the predicted arrivals times of Sdiff for 1D radial Earth model (PREM, Dziewonski and Anderson, 1981). Expected waveforms are computed synthetics for this 1D radial Earth model showing waveform variations predicted due to source effects, but little waveform complexities, due to the absence of any mantle heterogeneity in the model.

Event A (Fig. 2) is a shallow event, causing the depth phases (pSdiff and sSdiff) to arrive shortly after the main phase. The observed compared to the expected waveforms show evidence for deep 3D heterogeneity in two ways. Firstly, the initial Sdiff phases arrive later at smaller azimuths and earlier at larger azimuths. This variation in travel time is caused by the dichotomy in the lowermost mantle where the waves at smaller azimuths propagate through the LLVP beneath the Pacific, and the waves at larger azimuths propagate through broad areas of likely subducted slab material (Fig. 1). Secondly, and this is the focus of this study, delayed and significant postcursors are present. The postcursors interfere with the main arrivals at azimuths of 321-327° and move out in time towards larger azimuths. The nature of these postcursors is comparable to those observed for the Hawaiian and Icelandic mega-ULVZs (Cottaar and Romanowicz, 2012; Yuan and Romanowicz, 2017).

Event B (Fig. 3) shows comparable observations to event A. Again, the main Sdiff arrival shows a trend in arrival time with azimuth related to the LLVP boundary, and there is the presence of a postcursor that moves out towards larger azimuth with respect to the main Sdiff phases. However, the postcursor for this event is much weaker in amplitude relative to the main phase.

Event C (Fig. 4) shows postcursors with a very different propagation path through the same area at the core-mantle boundary. Its postcursors are stronger in amplitude towards larger azimuths and display a weaker move-out with time.

Event D (Fig. 5) shows hints of postcursor energy after the main phase at azimuths above 75°. Due to the poor station coverage in this area though, it is hard to observe any trends in the postcursor behavior. Potentially this data is also affected by a mega-ULVZ beneath the Marquesas as suggested by (Kim et al., 2020), implying there could be two postcursors. The data imaged by stations in the US at smaller azimuths show diffracted waves with no discernible postcursors, suggesting there are no mega-ULVZs located in a broad region of the core-mantle boundary between Hawaii and Marquesas.

3.2 Preferred model

Our best fitting ULVZ is centered at 105° W and 2° N. It has a height of 20 km and a width of 600 km, which is equal to nearly 10° on the core-mantle boundary. The

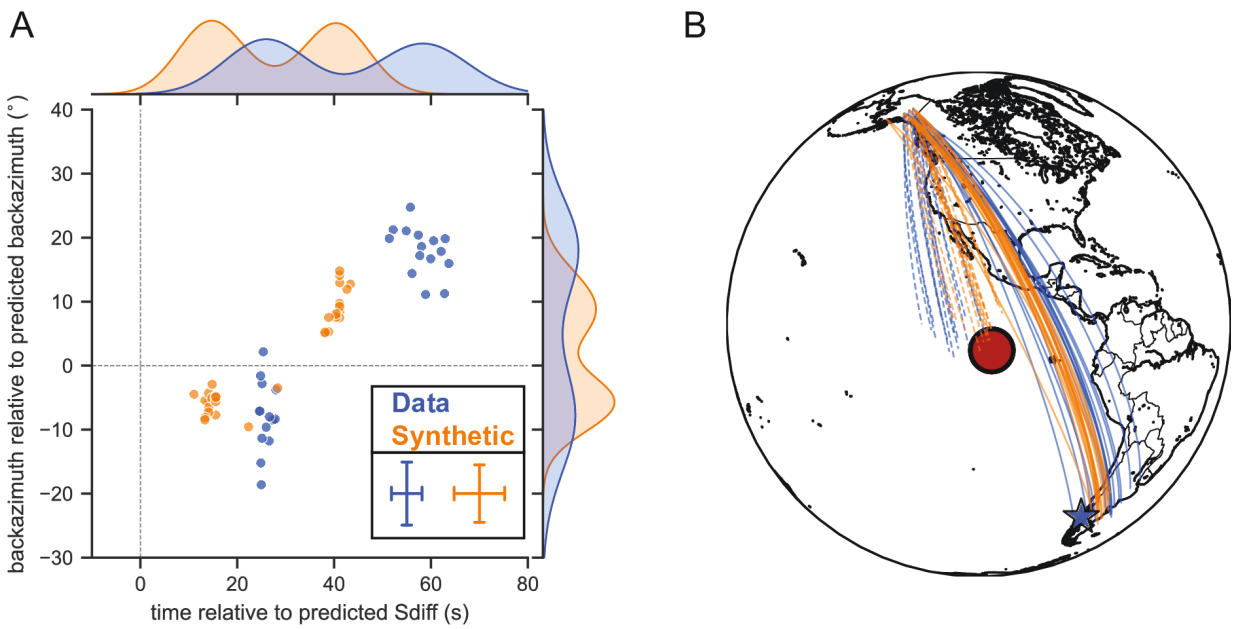

Figure 6 Beamforming results for event A. (A) Relative time versus relative backazimuth for picked peaks in beamform stack for real data (blue) and synthetic data for the ULVZ model (orange). Error bars in lower right shows median uncertainty for the observations. Note the bimodal distribution in both time and backazimuth related to the main and postcursor arrival. (B) Back-projection of determined backazimuths for energy peaks. Solid lines represent the main Sdiff arrival (defined as arrivals before 35 s), while the dashed lines represent the Sdiff postcursors (arrivals after 35s).

shear wave velocity within is reduced by 25% compared to surroundings. In Figs. 2-5, subplot B shows the wavefront predictions for this ULVZ model computed using a modified version of the wavefront tracker by (Hauser et al., 2008). Subplots E show the synthetic waveforms for the preferred ULVZ model. This reproduces the general move-out of the postcursors for Events A-C. It shows the relatively small amplitude postcursor for event B in comparison to event A, which is caused by the earthquake source of event B emitting relatively less shear energy in the direction of the ULVZ. For event C, the weaker move-out of the postcursor with time is predicted. For this event, the synthetics show clear and strong postcursors at smaller azimuths, which is not observed in the data. This could either mean that the assumed source mechanism is poor or that one side of the ULVZ has an irregular boundary or decreases in thickness.

Trade-offs and uncertainties do remain (see Supplementary Materials). Waveform results for shifted and resized ULVZ models are shown in the Figs. S6-S12 to illustrate the sensitivity of the data to various parameters. Based on these tests, estimated uncertainties on the preferred cylindrical model are at least 2° on location, 100 km in width, 5 km in height and 5% in velocity reduction.

3.3 Directionality of postcursors

Our preferred ULVZ model is confirmed by analyzing the directionality of the postcursor waveform by beamforming the energy for subarrays of stations where the main and postcursor are well separated. Fig. 6 shows the results for the significant postcursors present in event A, comparing the results for observations and synthetics. Both data and synthetics show a bimodal distribution of energy peaks, with the later cluster offset by 20-30° in backazimuth. Within error, the offset arrivals originate from the western boundary of the modeled ULVZ. There is an absolute time shift between the data and synthetics, which indicates unmodeled velocity variations along the Sdiff paths, but which are beyond the scope of this study. Beamforming results for other events are discussed in Supplementary Materials and for event C are shown in Fig. S14.

4 Discussion

The Galápagos ULVZ falls into the category of broad-scale mega-ULVZs, which are so far uncovered by diffracted phases. Other occurrences are mapped in 3D near Hawaii (Cottaar and Romanowicz, 2012; Jenkins et al., 2021; Lai et al., 2022; Li et al., 2022), Samoa (Thorne et al., 2013; Krier et al., 2021), and Iceland (Yuan and Romanowicz, 2017); these are shown in Fig. 7 combined with the global database of ULVZs by (Yu and Garnero, 2018). In general, a large variation of geometries of ULVZs has been suggested, and it is unclear if these all have comparable compositions and origins, and are shaped due to surrounding flows, or if these are distinctive features formed in different ways. To the south of the Galápagos Islands, for example, ULVZs have been mapped using PKP precursor phases that appear pile- or ridge-like with a width of 30 km and a height of 30 km (Ma et al., 2019), showing a very different aspect ratio from the mega-ULVZ observed here.

The edge of our preferred ULVZ location lies ~10° to the west of the Galápagos hotspot. A connection would require the Galápagos mantle plume to be offset in this direction. Seismic tomographic models identify low velocity anomalies beneath the Galápagos Islands, which

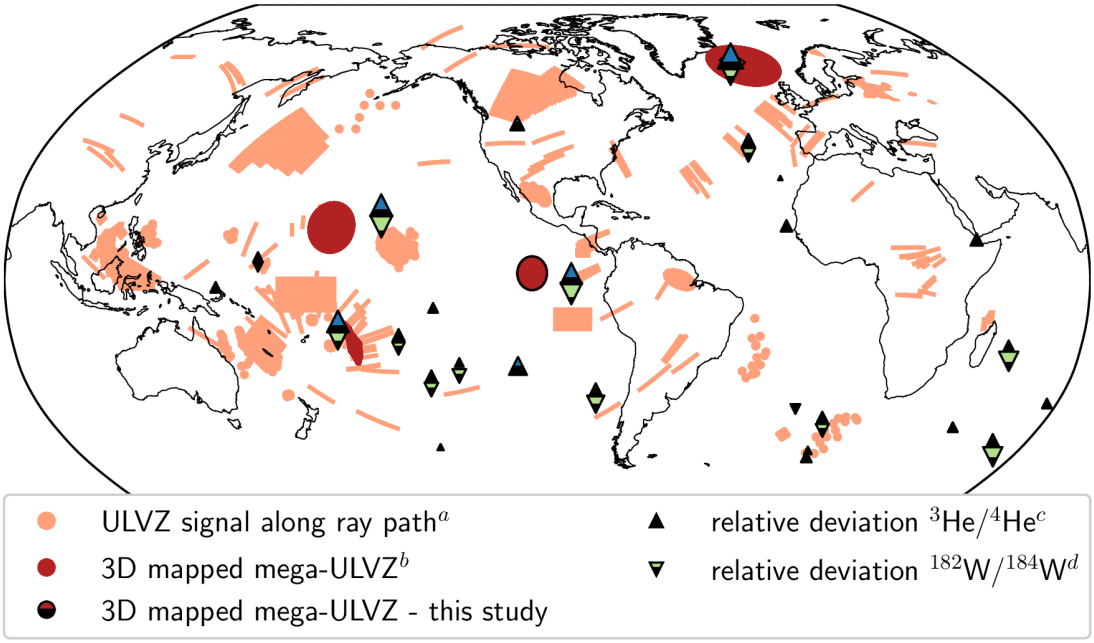

Figure 7 Mapped ULVZs and ocean island basalt isotopic signatures. Previous suggested locations of ULVZs (light orange) and recently 3D mapped mega-ULVZs (red) combined with helium and tungsten isotope ratio deviations observed in ocean island basalts compared to mid-ocean ridge basalts (scaled blue and green triangles, respectively). *a*. Compilation of ULVZ studies (Yu and Garnero, 2018) and a box is added for the region where small-scale ridges are found to the south of Galápagos Islands (Ma et al., 2019), *b*. Icelandic mega-ULVZ (Yuan and Romanowicz, 2017), Samoan mega-ULVZ from Thorne et al. (2013) and with 0.5 probability contour from Thorne et al. (2021), Hawaiian mega-ULVZ (Li et al., 2022). Note that other modeling studies for the mega-ULVZs near Hawaii (Jenkins et al., 2021; Lai et al., 2022; Li et al., 2022) and Samoa (Krier et al., 2021) not represented here. *c*. Scaled maximum observed positive $^{3}He/^{4}He$ isotopic ratio deviations from 9 Ra, the upper end of the MORB range, based on data compiled by Williams et al. (2019); Jackson et al. (2017); see references therein, and with additions from Jackson et al. (2020); Peters et al. (2021). *d*. Largest observed negative deviations in $\mu^{182}W$ compiled from Mundl et al. (2017); Rizo et al. (2019); Mundl-Petermeier et al. (2020). Note that the largest deviations for He and W do not always occur in the same samples for a given hotspot, and hotspots might be affected to different degrees by overprinting by recycled crust (Parai et al., 2019; Jackson et al., 2020; Péron et al., 2021; Day et al., 2022). Additionally, both the compilations of the ULVZs and the isotopic anomalies have a degree of geographical bias to where (more) studies have been conducted.

could be interpreted as plumes, but do not all agree on its direction of tilt or continuity across the mantle (Fig. 8). The resolution of the models beneath the Galápagos will be biased due to the seismic stations being largely located on land to the east and north. Some of the latest global mantle shear wave velocity models suggest the plume is offset to the southwest (French and Romanowicz, 2015; Lei et al., 2020) and this offset also results when combining shear velocity models with a geodynamical model (Williams et al., 2019). A recent innovative use of increasing coverage around the hotspot by using passively floating seismometers resulted in a P wave velocity model with a vertical plume down to 1900 km, beneath which resolution might be lost (Nolet et al., 2019). A different recent P wave velocity model focused on adding coverage in the lower mantle, observes a vertical plume down to 1000 km depth with fast velocities underneath (Hosseini et al., 2020). In both of these P wave models, the suggested plume is vertical. It is however easy to speculate that if there is a whole-mantle plume, that it originates within or at the edge of the LLVP (Steinberger and Torsvik, 2012; Li and Zhong, 2017) and its base is therefore offset to the west or southwest of the hotspot at the surface.

The geochemistry of basalts from the Galápagos archipelago indicate a plume with at least three distinct components, each manifesting in geographically-restricted portions of the archipelago along with a depleted upper mantle component (Harpp and White, 2001; Gleeson et al., 2021; Geist et al., 1988; White et al., 1993). Harpp and Weis (2020) observed that the plume component mixture evident in the southwestern part of the archipelago is distinct from that in the northeast and argued for a bilaterally asymmetric Galápagos plume. Notably, subaerial and submarine samples from the westernmost island of Fernandina exhibit the highest $^{3}He/^{4}He$ ratios in the archipelago (Graham et al., 1993; Kurz and Geist, 1999; Kurz et al., 2009), and the most solar-like Ne isotopic compositions of ocean islands globally (Kurz et al., 2009; Péron et al., 2021). Solar nebular helium and neon are thought to have dissolved into a terrestrial magma ocean during Earth's accretion (Harper and Jacobsen, 1996). High $^{3}He/^{4}He$ ratios in ocean island basalts (compared to those measured in mid-ocean ridge basalts) reflect greater retention of the primordial helium budget, which mutes the impact of radiogenic ^{4}He ingrowth by decay of U and Th over Earth history (Mukhopadhyay and Parai, 2019; Parai et al., 2019). The Fernandina helium and neon isotopic signatures indicate that the southwestern side of

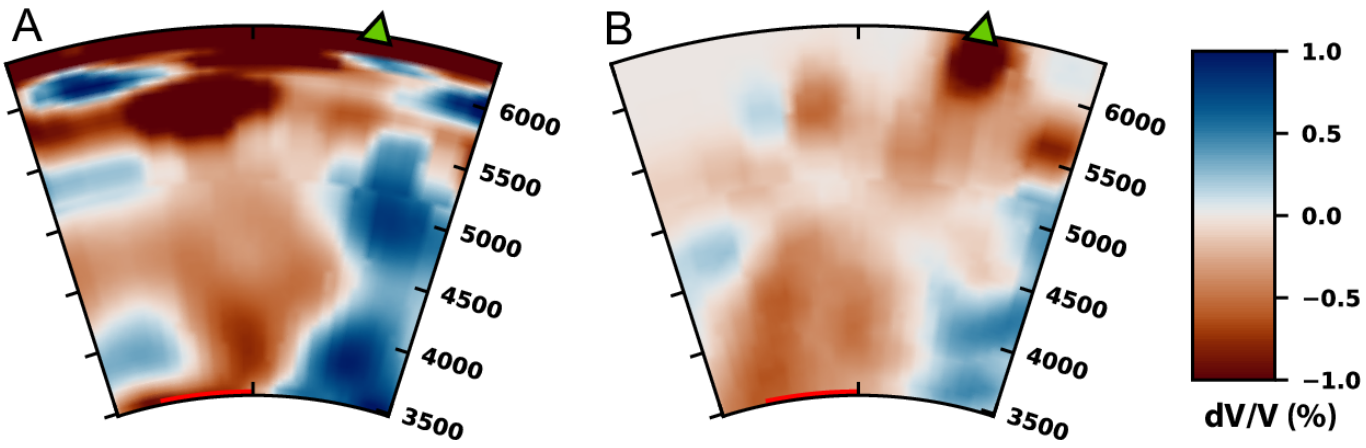

Figure 8 Cross-sections through the Galapagos ULVZ and hotspot. (A) Shear wave velocity deviations in SEMUCB-wm1 (French and Romanowicz, 2014). (B) P wave velocity deviations in DETOX-P2 (Hosseini et al., 2020). Red line on the core-mantle boundary shows location of ULVZ. Green triangle at the surface shows the location of hotspot. See Fig. 1 for location of the cross-section.

the Galápagos plume samples a reservoir that has experienced relatively little degassing and thus retained a high proportion of primordial solar He and Ne from Earth's accretion.

Four hotspot locations (Hawaii, Iceland, Samoa and Galápagos) that have a mega-ULVZ situated near their projection down onto the core-mantle boundary share a collective set of geochemical features. Samples from these locations exhibit high $^{3}He/^{4}He$ ratios, relatively solar-like Ne isotopes, and anomalous ^{182}W isotopic signatures (Fig. 7). ^{182}W was produced by decay of the extinct radionuclide ^{182}Hf in the first ~60 Myr of Earth history. Core segregation within the lifetime of ^{182}Hf fractionated Hf/W ratios and generated a radiogenic ^{182}W isotopic signature ($\mu^{182}W$=0, where $\mu^{182}W$ signifies the part per million deviation in $^{182}W/^{184}W$ from a laboratory standard) in the bulk silicate Earth compared to chondrites (Kleine et al., 2002; Yin et al., 2002). The core locked in an unradiogenic ^{182}W signature (negative $\mu^{182}W$), as would any other siderophile-enriched reservoir in the interior that formed during the lifetime of ^{182}Hf. Among hotspots, Hawaii, Iceland, Samoa, and Galápagos have the highest measured $^{3}He/^{4}He$ ratios (Kurz et al., 1983, 2009; Hilton et al., 1999; Jackson et al., 2007) and the most solar-like Ne isotopes (Valbracht et al., 1997; Trieloff et al., 2000; Kurz et al., 2009; Mukhopadhyay, 2012; Jackson et al., 2020; Péron et al., 2021; Peto et al., 2013). Some of the strongest negative $\mu^{182}W$ anomalies occur in samples with high $^{3}He/^{4}He$ ratios from these same hotspots (Mundl et al., 2017; Mundl-Petermeier et al., 2020, see Fig. 7).

The helium and neon isotopic signatures of the mega-ULVZ affiliated hotspots suggest a relatively undegassed source, which is commonly suggested to come from a deep mantle reservoir (Allègre et al., 1983; Parai et al., 2019), but has also been suggested to originate from the outer core (Bouhifd et al., 2020). Xe isotopes measured in samples with high $^{3}He/^{4}He$ and solar-like Ne from Iceland and Samoa require that the reservoir that hosts this signature separated from the upper mantle within the first ~100 Myr of Earth history (Mukhopadhyay, 2012; Peto et al., 2013). The anomalous tungsten isotope signature (negative $\mu^{182}W$) suggests the involvement of a siderophile-enriched reservoir that likewise formed early in Earth's history. An obvious candidate for this reservoir is the core, and many potential processes to transfer material or isotopic signatures across the core-mantle boundary have been proposed (Kanda and Stevenson, 2006; Hayden and Watson, 2007; Otsuka and Karato, 2012; Lesher et al., 2020; Buffett et al., 2000; Lim et al., 2021). However, direct material transfer from the core would impart strongly fractionated noble gas elemental ratios to a plume, and these are not observed (Wang et al., 2022). An alternative is an early-formed, iron-rich deep mantle reservoir. Mundl-Petermeier et al. (2020) suggests that to explain the full space of helium-tungsten isotope observations, two high $^{3}He/^{4}He$ components are needed: one with negative $\mu^{182}W$ and one with tungsten isotopes similar to the bulk silicate Earth. These distinct components could potentially reflect material entrainment from an LLVP and a ULVZ, with the ULVZ providing the negative tungsten isotope signature. Geodynamical modeling shows mantle plumes can sample LLVP material, and to a degree the much denser ULVZ material (Jones et al., 2019). The correlation between these mega-ULVZs and the isotopic signatures is striking and should be tested in further localities.

5 Conclusion

We present seismic evidence of a mega-ULVZ on the core-mantle boundary to the west of the Galápagos Islands in the form of postcursors to the Sdiff phase. Modeling the delay times and move-out of the postcursors allows us to constrain a simplified cylindrical shape with a width of ~600 km, a height of 20 km, a shear wave velocity reduction of 25%, and centered at 105° W and 2° N. This model also largely reproduces the observed incoming directionality of the postcursors. Similar mega-ULVZs have been mapped beneath or near the Hawaiian, Samoan and Icelandic hotspots. Ocean island basalts in all four locations show anomalous signatures in He, Ne, and W, which could be clues to

the mega-ULVZs representing a primordial reservoir or containing a component of outer core material.

Acknowledgements

The authors thank Curtis Williams, Helen Williams, and Vedran Lekić for discussion of this work. SC, CM, and ZL were funded by the European Research Council (ERC) under the European Union's Horizon 2020 research and innovation programme (grant agreement No. 804071 -ZoomDeep). RP was funded by National Science Foundation grant EAR 2145663. This work was performed using resources provided by the Cambridge Service for Data Driven Discovery (CSD3) operated by the University of Cambridge Research Computing Service (www.csd3.cam.ac.uk).

Data and code availability

Processed and quality controlled observed data, synthetic data, and codes for data processing and plotting are available at https://doi.org/10.5281/zenodo.7229683. Processing scripts make use of ObsPy (www.obspy.org). We use sandwiched-CSEM (Capdeville et al., 2003) to compute the synthetics; contact the authors of that study for access. Cross-sections for Figure 7 are taken from Submachine (http://www.earth.ox.ac.uk/~smachine/). The facilities of IRIS Data Services (www.iris.edu), and specifically the IRIS Data Management Center, were used for access to waveforms and related metadata. IRIS Data Services are funded through the Seismological Facilities for the Advancement of Geoscience (SAGE) Award of the National Science Foundation under Cooperative Support Agreement EAR-1851048. Data from the TA network were made freely available as part of the EarthScope USArray facility, operated by Incorporated Research Institutions for Seismology (IRIS) and supported by the National Science Foundation, under Cooperative Agreements EAR-1261681. Earthquake parameters were used from the Global CMT Project (www.globalcmt.org) and USGS National Earthquake Information Centre (earthquake.usgs.gov).

References

Allègre, C., Staudacher, T., Sarda, P., and Kurz, M. Constraints on evolution of Earth's mantle from rare gas systematics. *Nature*, 303(5920):762–766, 1983. doi: 10.1038/303762a0.

Bouhifd, M., Jephcoat, A., Porcelli, D., Kelley, S., and Marty, B. Potential of Earth's core as a reservoir for noble gases: Case for helium and neon. *Geochemical Perspectives Letters*, 15:15–18, 2020. doi: 10.7185/geochemlet.2028.

Buffett, B., Garnero, E., and Jeanloz, R. Sediments at the Top of Earth's Core. *Science*, 290(5495):1338–1342, 2000. doi: 10.1126/science.290.5495.1338.

Capdeville, Y., Larmat, C., Vilotte, J.-P., and Montagner, J.-P. A new coupled spectral element and modal solution method for global seismology: A first application to the scattering induced by a plume-like anomaly. *Geophysical Research Letters*, 29(9): 32–1–32–4, 2002. doi: 10.1029/2001GL013747.

Capdeville, Y., To, A., and Romanowicz, B. Coupling spectral elements and modes in a spherical Earth: an extension to the "sandwich" case. *Geophysical Journal International*, 154(1): 44–57, 2003. doi: 10.1046/j.1365-246X.2003.01959.x.

Cottaar, S. and Lekić, V. Morphology of seismically slow lower-mantle structures. *Geophys. J. Int*, 207(2):1122–1136, 2016. doi: 10.1093/gji/ggw324.

Cottaar, S. and Romanowicz, B. An unsually large ULVZ at the base of the mantle near Hawaii. *Earth and Planetary Science Letters*, 355–356:213–222, 2012. doi: 10.1016/j.epsl.2012.09.005.

Dannberg, J., Myhill, R., Gassmöller, R., and Cottaar, S. The morphology, evolution and seismic visibility of partial melt at the core-mantle boundary: Implications for ULVZs. *Geophysical Journal International*, 227(2):1028–1059, 2021. doi: 10.1093/gji/ggab242.

Day, J., Jones, T., and Nicklas, R. Mantle sources of ocean islands basalts revealed from noble gas isotope systematics. *Chemical Geology*, 587:120626, 2022. doi: 10.1016/j.chemgeo.2021.120626.

Dobrosavljevic, V., Sturhahn, W., and Jackson, J. Evaluating the role of iron-rich (Mg,Fe)O in ultralow velocity zones. *Minerals*, 9 (12):762, 2019. doi: 10.3390/min9120762.

Domeier, M., Doubrovine, P., Torsvik, T., Spakman, W., and Bull, A. Global correlation of lower mantle structure and past subduction. *Geophysical Research Letters*, 43(10):4945–4953, 2016. doi: 10.1002/2016GL068827.

Dziewonski, A. and Anderson, D. Preliminary reference Earth model. *Physics of the Earth and Planetary Interiors*, 25(4): 297–356, 1981. doi: 10.1016/0031-9201(81)90046-7.

Ekström, G., Nettles, M., and Dziewoński, A. The global CMT project 2004-2010: Centroid-moment tensors for 13,017 Earthquakes. *Physics of the Earth and Planetary Interiors*, 200–201:1–9, 2012. doi: 10.1016/j.pepi.2012.04.002.

French, S. and Romanowicz, B. Whole-mantle radially anisotropic shear velocity structure from spectral-element waveform tomography. *Geophysical Journal International*, 199(3): 1303–1327, 2014. doi: 10.1093/gji/ggu334.

French, S. and Romanowicz, B. Broad plumes rooted at the base of the Earth's mantle beneath major hotspots. *Nature*, 525(7567): 95–9, 2015. doi: 10.1038/nature14876.

Garnero, E., McNamara, A., and Shim, S.-H. Continent-sized anomalous zones with low seismic velocity at the base of Earth's mantle. *Nature Geosci*, 9(7):481–489, 2016. doi: 10.1038/ngeo2733.

Geist, D., White, W., and McBirney, A. Plume-asthenosphere mixing beneath the Galapagos archipelago. *Nature*, 333(6174): 657–660, 1988. doi: 10.1038/333657a0.

Gleeson, M., Soderman, C., Matthews, S., Cottaar, S., and Gibson, S. Geochemical Constraints on the Structure of the Earth's Deep Mantle and the Origin of the LLSVPs. *Geochemistry, Geophysics, Geosystems*, 22(9), 2021. doi: 10.1029/2021GC009932.

Graham, D., Christie, D., Harpp, K., and Lupton, J. Mantle plume helium in submarine basalts from the Galápagos platform. *Science*, 262(5142):2023–2026, 1993. doi: 10.1126/science.262.5142.2023.

Harper, C. and Jacobsen, S. Noble gases and Earth's accretion. *Science*, 273(5283):1814–1818, 1996. doi: 10.1126/science.273.5283.1814.

Harpp, K. and Weis, D. Insights Into the Origins and Compositions of Mantle Plumes: A Comparison of Galápagos and Hawai'i. *Geochemistry, Geophysics, Geosystems*, 21(9), 2020. doi: 10.1029/2019GC008887.

Harpp, K. and White, W. Tracing a mantle plume: Iso-

topic and trace element variations of Galápagos seamounts. *Geochemistry, Geophysics, Geosystems*, 2(6), 2001. doi: 10.1029/2000gc000137.

Hauser, J., Sambridge, M., and Rawlinson, N. Multiarrival wavefront tracking and its applications. *Geochemistry, Geophysics, Geosystems*, 9(11), 2008. doi: 10.1029/2008GC002069.

Hayden, L. and Watson, E. A diffusion mechanism for core–mantle interaction. *Nature*, 450(7170):709–711, 2007. doi: 10.1038/nature06380.

Hernlund, J. and Jellinek, A. Dynamics and structure of a stirred partially molten ultralow-velocity zone. *Earth and Planetary Science Letters*, 296(1–2):1–8, 2010. doi: 10.1016/j.epsl.2010.04.027.

Hilst, R., Widiyantoro, S., and Engdahl, E. Evidence for deep mantle circulation from global tomography. *Nature*, 386(6625): 578–584, 1997. doi: 10.1038/386578a0.

Hilton, D., Grönvold, K., Macpherson, C., and Castillo, P. Extreme 3He/4He ratios in northwest Iceland: Constraining the common component in mantle plumes. *Earth and Planetary Science Letters*, 173(1–2):53–60, 1999. doi: 10.1016/S0012-821X(99)00215-0.

Hosseini, K., Sigloch, K., Tsekhmistrenko, M., Zaheri, A., Nissen-Meyer, T., and Igel, H. Global mantle structure from multifrequency tomography using P, PP and P-diffracted waves. *Geophysical Journal International*, 220(1):96–141, 2020. doi: 10.1093/gji/ggz394.

Jackson, M., Kurz, M., Hart, S., and Workman, R. New Samoan lavas from Ofu Island reveal a hemispherically heterogeneous high 3He/4He mantle. *Earth and Planetary Science Letters*, 264 (3–4):360–374, 2007. doi: 10.1016/j.epsl.2007.09.023.

Jackson, M., Konter, J., and Becker, T. Primordial helium entrained by the hottest mantle plumes. *Nature*, 542(7641):340–343, 2017. doi: 10.1038/nature21023.

Jackson, M., Blichert-Toft, J., Halldórsson, S., Mundl-Petermeier, A., Bizimis, M., Kurz, M., Price, A., Haroardóttir, S., Willhite, L., Breddam, K., Becker, T., and Fischer, R. Ancient helium and tungsten isotopic signatures preserved in mantle domains least modified by crustal recycling. *Proceedings of the National Academy of Sciences of the United States of America*, 117(49): 30993–31001, 2020. doi: 10.1073/pnas.2009663117.

Jellinek, A. and Manga, M. Links between long-lived hot spots, mantle plumes, D'' , and plate tectonics. *Reviews of Geophysics*, 42(3):3002, 2004. doi: 10.1029/2003RG000144.

Jenkins, J., Mousavi, S., Li, Z., and Cottaar, S. A high-resolution map of Hawaiian ULVZ morphology from ScS phases. *Earth and Planetary Science Letters*, 563:116885, 2021. doi: 10.1016/j.epsl.2021.116885.

Jones, T., Davies, D., and Sossi, P. Tungsten isotopes in mantle plumes: Heads it's positive, tails it's negative. *Earth and Planetary Science Letters*, 506:255–267, 2019. doi: 10.1016/J.EPSL.2018.11.008.

Kanda, R. and Stevenson, D. Suction mechanism for iron entrainment into the lower mantle. *Geophys. Res. Lett*, 33(2):02310, 2006. doi: 10.1029/2005GL025009.

Kim, D., Lekić, V., Ménard, B., Baron, D., and Taghizadeh-Popp, M. Sequencing seismograms: A panoptic view of scattering in the core-mantle boundary region. *Science*, 368(6496):1223–1228, 2020. doi: 10.1126/science.aba8972.

Kleine, T., Münker, C., Mezger, K., and Palme, H. Rapid accretion and early core formation on asteroids and the terrestrial planets from Hf-W chronometry. *Nature*, 418(6901):952–955, 2002. doi: 10.1038/nature00982.

Krier, J., Thorne, M., Leng, K., and Nissen-Meyer, T. A Compositional Component to the Samoa Ultralow-Velocity Zone Revealed Through 2- and 3-D Waveform Modeling of SKS and SKKS Differential Travel-Times and Amplitudes. *Journal of Geophysical Research: Solid Earth*, 126(7):2021 021897, 2021. doi: 10.1029/2021JB021897.

Kurz, M. and Geist, D. Dynamics of the Galapagos hotspot from helium isotope geochemistry. *Geochimica et Cosmochimica Acta*, 63(23–24):4139–4156, 1999. doi: 10.1016/s0016-7037(99)00314-2.

Kurz, M., Jenkins, W., Hart, S., and Clague, D. Helium isotopic variations in volcanic rocks from Loihi Seamount and the Island of Hawaii. *Earth and Planetary Science Letters*, 66(C):388–406, 1983. doi: 10.1016/0012-821X(83)90154-1.

Kurz, M., Curtice, J., Fornari, D., Geist, D., and Moreira, M. Primitive neon from the center of the Galápagos hotspot. *Earth and Planetary Science Letters*, 286(1–2):23–34, 2009. doi: 10.1016/j.epsl.2009.06.008.

Labrosse, S., Hernlund, J., and Coltice, N. A crystallizing dense magma ocean at the base of the Earth's mantle. *Nature*, 450 (7171):866–9, 2007. doi: 10.1038/nature06355.

Lai, V., Helmberger, D., Dobrosavljevic, V., Wu, W., Sun, D., Jackson, J., and Gurnis, M. Strong ULVZ and Slab Interaction at the Northeastern Edge of the Pacific LLSVP Favors Plume Generation. *Geochemistry, Geophysics, Geosystems*, 23(2), 2022. doi: 10.1029/2021gc010020.

Lei, W., Ruan, Y., Bozdağ, E., Peter, D., Lefebvre, M., Komatitsch, D., Tromp, J., Hill, J., Podhorszki, N., and Pugmire, D. Global adjoint tomography - Model GLAD-M25. *Geophysical Journal International*, 223(1):1–21, 2020. doi: 10.1093/gji/ggaa253.

Lesher, C., Dannberg, J., Barfod, G., Bennett, N., Glessner, J., Lacks, D., and Brenan, J. Iron isotope fractionation at the core–mantle boundary by thermodiffusion. *Nature Geoscience*, 13(5): 382–386, 2020. doi: 10.1038/s41561-020-0560-y.

Li, J., Sun, D., and Bower, D. Slab control on the mega-sized North Pacific ultra-low velocity zone. *Nature Communications*, 13(1): 1042, 2022. doi: 10.1038/s41467-022-28708-8.

Li, M. and Zhong, S. The source location of mantle plumes from 3D spherical models of mantle convection. *Earth and Planetary Science Letters*, 478:47–57, 2017. doi: 10.1016/J.EPSL.2017.08.033.

Li, M., McNamara, A., Garnero, E., and Yu, S. Compositionally-distinct ultra-low velocity zones on Earth's core-mantle boundary. *Nature comm*, 8(1):177, 2017. doi: 10.1038/s41467-017-00219-x.

Lim, K., Bonati, I., and Hernlund, J. A Hybrid Mechanism for Enhanced Core-Mantle Boundary Chemical Interaction. *Geophysical Research Letters*, 48(23), 2021. doi: 10.1029/2021GL094456.

Ma, X., Sun, X., and Thomas, C. Localized ultra-low velocity zones at the eastern boundary of Pacific LLSVP. *Earth and Planetary Science Letters*, 507:40–49, 2019. doi: 10.1016/J.EPSL.2018.11.037.

Mukhopadhyay, S. Early differentiation and volatile accretion recorded in deep-mantle neon and xenon. *Nature*, 486(7401): 101–104, 2012. doi: 10.1038/nature11141.

Mukhopadhyay, S. and Parai, R. Noble gases: A record of Earth's evolution and mantle dynamics. *Annual Review of Earth and Planetary Sciences. Annual Reviews*, page 389–419, 2019. doi: 10.1146/annurev-Earth-053018-060238.

Mundl, A., Touboul, M., Jackson, M., Day, J., Kurz, M., Lekic, V., Helz, R., and Walker, R. Tungsten-182 heterogeneity in modern ocean island basalts. *Science*, 356(6333):66–69, 2017. doi: 10.1126/science.aal4179.

Mundl-Petermeier, A., Walker, R., Fischer, R., Lekic, V., Jackson, M., and Kurz, M. Anomalous 182W in high 3He/4He ocean island

basalts: Fingerprints of Earth's core? *Geochimica et Cosmochimica Acta*, 271:194–211, 2020. doi: 10.1016/j.gca.2019.12.020.

Nolet, G., Hello, Y., Lee, S. d., Bonnieux, S., Ruiz, M., Pazmino, N., Deschamps, A., Regnier, M., Font, Y., Chen, Y., and Simons, F. Imaging the Galápagos mantle plume with an unconventional application of floating seismometers. *Scientific Reports*, 9(1): 1326, 2019. doi: 10.1038/s41598-018-36835-w.

Otsuka, K. and Karato, S. Deep penetration of molten iron into the mantle caused by a morphological instability. *Nature*, 492 (7428):243–246, 2012. doi: 10.1038/nature11663.

Parai, R., Mukhopadhyay, S., Tucker, J., and Pető, M. The emerging portrait of an ancient, heterogeneous and continuously evolving mantle plume source. *Lithos. Elsevier*, page 105153, 2019. doi: 10.1016/j.lithos.2019.105153.

Peters, B., Mundl-Petermeier, A., Carlson, R., Walker, R., and Day, J. Combined Lithophile-Siderophile Isotopic Constraints on Hadean Processes Preserved in Ocean Island Basalt Sources. *Geochemistry, Geophysics, Geosystems*, 22(3), 2021. doi: 10.1029/2020GC009479.

Peto, M., Mukhopadhyay, S., and Kelley, K. Heterogeneities from the first 100 million years recorded in deep mantle noble gases from the Northern Lau Back-arc Basin. *Earth and Planetary Science Letters*, 369–370:13–23, 2013. doi: 10.1016/j.epsl.2013.02.012.

Péron, S., Mukhopadhyay, S., Kurz, M., and Graham, D. Deep-mantle krypton reveals Earth's early accretion of carbonaceous matter. *Nature*, 600(7889):462–467, 2021. doi: 10.1038/s41586-021-04092-z.

Rizo, H., Andrault, D., Bennett, N., Humayun, M., Brandon, A., Vlastelic, I., Moine, B., Poirier, A., Bouhifd, M., and Murphy, D. 182W evidence for core-mantle interaction in the source of mantle plumes. *Geochemical Perspectives Letters*, 11:6–11, 2019. doi: 10.7185/geochemlet.1917.

Rost, S. and Thomas, C. Array seismology: Methods and applications. *Reviews of Geophysics*, 40(3):1008, 2002. doi: 10.1029/2000RG000100.

Schimmel, M. and Paulssen, H. Noise reduction and detection of weak, coherent signals through phase-weighted stacks. *Geophysical Journal International*, 130(2):497–505, 1997. doi: 10.1111/j.1365-246X.1997.tb05664.x.

Steinberger, B. and Torsvik, T. A geodynamic model of plumes from the margins of Large Low Shear Velocity Provinces. *Geochemistry, Geophysics, Geosystems*, 13(1):–, 2012. doi: 10.1029/2011GC003808.

Thorne, M., Garnero, E., Jahnke, G., Igel, H., and McNamara, A. Mega ultra low velocity zone and mantle flow. *Earth and Planetary Science Letters*, 364:59–67, 2013. doi: 10.1016/j.epsl.2012.12.034.

Thorne, M., Pachhai, S., Leng, K., Wicks, J., and Nissen-Meyer, T. New Candidate Ultralow-Velocity Zone Locations from Highly Anomalous SPdKS Waveforms. *Minerals*, 10(3):211, 2020. doi: 10.3390/min10030211.

Thorne, M., Leng, K., Pachhai, S., Rost, S., Wicks, J., and Nissen-Meyer, T. The Most Parsimonious Ultralow-Velocity Zone Distribution From Highly Anomalous SPdKS Waveforms. *Geochemistry, Geophysics, Geosystems*, 22(1):2020 009467, 2021. doi: 10.1029/2020GC009467.

Trieloff, M., Kunz, J., Clague, D., Harrison, D., and Allègre, C. The nature of pristine noble gases in mantle plumes. *Science*, 288 (5468):1036–1038, 2000. doi: 10.1126/science.288.5468.1036.

Valbracht, P., Staudacher, T., Malahoff, A., and Allègre, C. Noble gas systematics of deep rift zone glasses from Loihi Seamount, Hawaii. *Earth and Planetary Science Letters*, 150(3–4):399–411, 1997. doi: 10.1016/s0012-821x(97)00094-0.

Wang, K., Lu, X., Liu, X., Zhou, M., and Yin, K. Partitioning of noble gases (He, Ne, Ar, Kr, Xe) during Earth's core segregation: A possible core reservoir for primordial noble gases. *Geochimica et Cosmochimica Acta*, 321:329–342, 2022. doi: 10.1016/j.gca.2022.01.009.

White, W., McBirney, A., and Duncan, R. Petrology and geochemistry of the Galapagos Islands: portrait of a pathological mantle plume. *Journal of Geophysical Research*, 98(B11):19533–19563, 1993. doi: 10.1029/93jb02018.

Wicks, J., Jackson, J., Sturhahn, W., and Zhang, D. Sound velocity and density of magnesiowüstites: Implications for ultralow-velocity zone topography. *Geophysical Research Letters*, 44(5): 2148–2158, 2017. doi: 10.1002/2016GL071225.

Williams, C., Mukhopadhyay, S., Rudolph, M., and Romanowicz, B. Primitive Helium Is Sourced From Seismically Slow Regions in the Lowermost Mantle. *Geochemistry, Geophysics, Geosystems*, 20(8):4130–4145, 2019. doi: 10.1029/2019GC008437.

Yin, Q., Jacobsen, S., Yamashita, K., Blichert-Toft, J., Télouk, P., and Albarède, F. A short timescale for terrestrial planet formation from Hf-W chronometry of meteorites. *Nature*, 418(6901): 949–952, 2002. doi: 10.1038/nature00995.

Yu, S. and Garnero, E. Ultralow Velocity Zone Locations: A Global Assessment. *Geochemistry, Geophysics, Geosystems*, 19 (2):396–414, 2018. doi: 10.1002/2017GC007281.

Yuan, K. and Romanowicz, B. Seismic evidence for partial melting at the root of major hot spot plumes. *Science*, 357:393–397, 2017. doi: 10.1126/science.aan0760.